Recombination, gain, band structure, efficiency, and reliability of 1.5-μm GaInNAsSb/GaAs lasers

Lynford L. Goddard,[a] Seth R. Bank, Mark A. Wistey, Homan B. Yuen, Zhilong Rao, and James S. Harris, Jr.
Solid State and Photonics Laboratory, Stanford University, Stanford, California 94305

(Received 27 October 2004; accepted 19 January 2005; published online 4 April 2005)

We present temperature-dependent measurements of the local Z parameter, which reflects the dominant recombination processes. At room temperature, Z increases with current from 1.2 at low bias up to a threshold value, Z_{th}, of only 2.0, demonstrating the existence of significant amounts of monomolecular recombination. At elevated temperatures, Z_{th} rises above 2.5. We calculate the laser's band diagram and estimate 35 meV of band-gap renormalization at threshold through polarization-resolved measurements of exciton peaks in the absorption spectrum and inflection points of the absorption, spontaneous emission, and gain spectra. The small effective valence-band barrier height of 115 meV leads to hole leakage due to thermionic emission and carrier spillover into the barriers. This could explain the increase in Z_{th} at elevated temperatures and decrease in internal quantum efficiency from 57% at 15 °C to 47% at 75 °C. We also analyze the spontaneous emission and gain spectra below and above threshold. The spontaneous emission clamped rather weakly at threshold, which also partially explains the low internal efficiency at room temperature. We present initial reliability measurements of over 100 h at 10-mW continuous-wave power from a single facet. After 50 h of life testing, the threshold current increased by 79% and the external differential quantum efficiency decreased by 39% of their respective pretest values. By comparing the local Z parameter versus current-density curves before and after life testing, we have identified an increase in monomolecular recombination as the main source of degraded device performance. © *2005 American Institute of Physics*. [DOI: 10.1063/1.1873035]

INTRODUCTION

Recently, the lasing wavelength of high-power continuous-wave (cw) GaInNAs(Sb) lasers grown on GaAs by molecular-beam epitaxy (MBE) has been extended up to 1.52 μm (Ref. 1) in an effort to cover the entire telecommunication band of 1.2–1.6 μm and replace InP-based devices. Lasers based on GaAs have several advantages over InP: lower cost wafers, less temperature sensitivity, fewer mirror pairs in distributed Bragg reflectors for vertical-cavity surface-emitting lasers (VCSELs), and native oxide apertures for current confinement. At room temperature, typical GaInNAsSb single quantum well (SQW) edge-emitting lasers at 1.5 μm achieve single-facet cw output power exceeding 100 mW, threshold densities below 1.1 kA/cm^2, and a characteristic temperature, T_0, above 100 K.[2] Further, pulsed VCSELs operating at 1.46 μm have been demonstrated at −10 °C.[3] Most recently, 580-A/cm^2 threshold density and 200-mW dual facet power have been realized[4] by reducing monomolecular recombination.[5] In addition, Infineon has reported GaInNAs/GaAs lasers at 1.59 μm.[6] In this paper, we present recombination measurements for GaInNAsSb lasers at 1.5 μm for comparison with existing reports for GaInNAs/GaAs at 1.3 μm and InGaAsP/InP at 1.3 and 1.5 μm.[7–9] We also report on gain, band structure, and reliability at 1.5 μm for comparison with GaInNAs/GaAs at 1.3 μm (Refs. 10–13) and InGaAsP/InP at 1.3 and 1.5 μm.[14–16]

[a]Electronic mail: lgoddard@snow.stanford.edu

SPONTANEOUS EMISSION

Measurement techniques

A quick and useful method for studying carrier recombination and internal efficiency is measurement of the spontaneous emission spectrum below and above threshold. SQW ridge-waveguide edge-emitting lasers, with 22-nm $GaN_{0.025}As_{0.975}$ barriers and a 7.8-nm $Ga_{0.62}In_{0.38}N_{0.023}As_{0.950}Sb_{0.027}$ active region, whose growth, fabrication, and performance details are described elsewhere,[1,2] were soldered episide up to a temperature-controlled copper heat sink. The vertically emitted, unamplified, true spontaneous emission (TSE) of the laser device was collimated using a lens with a moderate numerical aperture (NA=0.31). This limits the collection angle inside the active region to $<5°$ due to refraction from the high index layers to air. The light was focused onto a multimode fiber for measurement with an optical spectrum analyzer (OSA). The TSE escaped the device structure vertically around the ridge-waveguide metal edges in one setup, labeled EDGE in Fig. 1, and through a 5×10 μm^2 window that was etched in the top p metal and slightly into the p-AlGaAs cladding layer using a focused ion beam (FIB) in another setup, labeled WINDOW also shown in Fig. 1. In WINDOW mode, some of the EDGE light will also be detected. Unless otherwise mentioned, data pertain to lasers with a highly reflective (HR) coating (R=98.7%) on one facet and as-cleaved (R=30%) on the other.

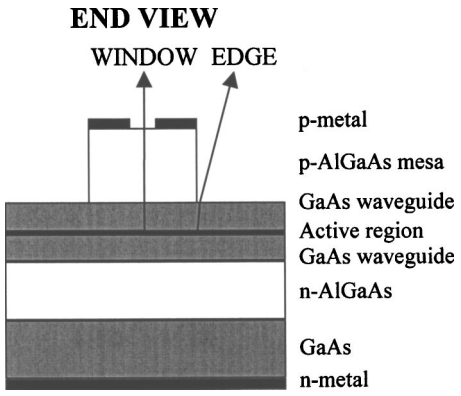

FIG. 1. WINDOW and EDGE measurement configurations for TSE.

By design, the polarization of the collected light in this vertical configuration is transverse electric (TE). Transverse magnetic (TM) can only be emitted in the quantum well (QW) plane. Since the GaInNAsSb quantum well is compressively strained on GaAs at ≈2.5%, the main interband transition is between the ground states of the electron and heavy hole $(E^1\text{-}HH^1)_{QW}$, which has nonzero transition matrix elements for TE polarization only. Therefore, a fixed fraction of all of the emission of the main transition was collected in this configuration. Since the GaNAs barriers are tensilely strained on GaAs at ≈0.5%, the lowest interband transition in the barriers is between the continuum of states of the electron and light hole $(E\text{-}LH)_{Barrier}$. Both TE and TM polarized emission exist in plane, but only the TE portion of the main barrier transition is detected vertically. As we shall see in the absorption section, the compressive strain in the well coupled with the tensile strain in the barrier prevents the light holes from having quantized levels in the QW for our GaInNAsSb/GaNAs compositions. Instead, the QW acts as a small perturbation to the potential of the barrier. The light holes form a continuum, with a quasi-three-dimensional (3D) density of states since the total width of the barrier plus QW is 51.8 nm. However, they may accumulate at the barrier/well interfaces because of the Coulomb attraction to the electrons in the QW.

The small collection angle of $<5°$ produced low signal levels so the data were collected in cw and pulsed (1-μs width, 10% duty cycle) modes. Unfortunately, this leads to device heating of about 30 °C in cw and 3 °C in pulsed mode at 3 kA/cm^2. We will denote the stage and active region temperatures by T_s and T_a, respectively. The thermal resistance, R_T, of our devices has been extensively measured.[2] For 20-μm-wide devices, the resistance in K/W is well modeled by $R_T=30.3/L$, where L is the device length in millimeters. Some measurements were made in cw mode to increase the span of the spectra or to improve the accuracy of the applied current. Background subtraction was performed on all raw spectra to further improve measurement sensitivity.

The collection efficiency was wavelength dependent due to the chromatic aberration in the lenses and the wavelength dependence of refraction and Fresnel transmission arising from the dispersion of the refractive index of the active region. However, these effects are estimated to reduce the overall measurement accuracy by $<7\%$. OSA spectra, which measure power within a resolution bandwidth, ResBW: $P(\lambda)$ResBW, were converted to emission rates in photons per second per unit energy by dividing by E^3ResBW/(hc), where E is the photon energy, h is Planck's constant, and c is the speed of light.

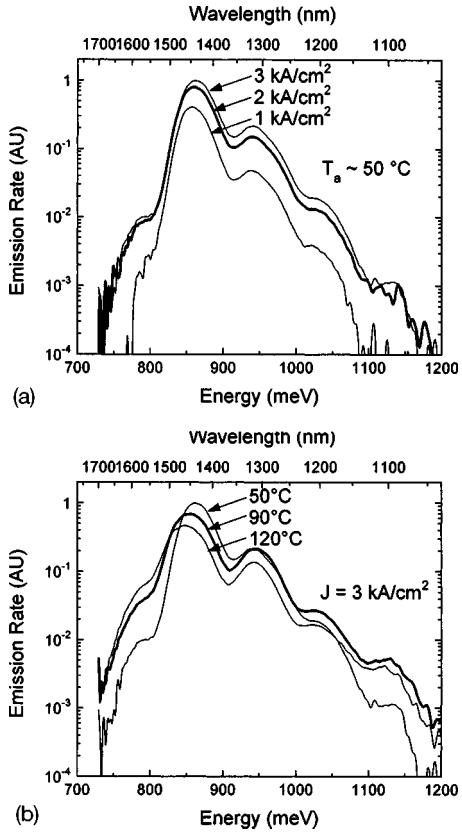

FIG. 2. TSE-WINDOW spectra after background subtraction and FFT smoothing filter for a 20×306 μm^2 device. (a) is at $T_a\approx50$ °C for 1, 2, and 3 kA/cm^2 while (b) is at 3 kA/cm^2 for $T_a\approx50$, 90, and 120 °C.

Results and discussion

The TSE-WINDOW spectra were measured on a 20×306 μm^2 device. The short device had high enough mirror loss that cw lasing was not observed. This allowed the application of large current densities in order to observe higher-order transitions. However, the short length of the device led to a large thermal resistance of 96 K/W. The spectra for 1, 2, and 3 kA/cm^2 at $T_a\approx50$ °C ($T_s=45$, 25, 5 °C) are plotted in Fig. 2(a), while the spectra for 3 kA/cm^2 at $T_a=50$, 90, and 120 °C ($T_s=5$, 45, 85 °C) are displayed in Fig. 2(b). A post-measurement, high-frequency, fast Fourier transform (FFT) smoothing filter was applied to the data with a bandwidth that was narrower than the OSA resolution bandwidth to further reduce background noise without sacrificing spectral features.

For comparison with other measurements to be presented in later sections, we will discuss the data for 2 kA/cm^2 at $T_a\approx35$ °C (not shown in Fig. 2, but similar). The peaks at 863 ± 2, 942 ± 3, and 1022 ± 7 meV are attributed primarily to the broad overlapping peaks of the dominant QW transitions from the two electron levels to the three heavy-hole levels: E^1-HH^1, E^1-HH^3, and E^2-HH^2, while the

peak at 1114±8 meV is attributed to barrier emission, $(E\text{-}LH)_{Barrier}$. From TM spectra, presented in the multisection emission section, a small portion of the emission on the high-energy side of the 942- and 1022-meV peaks is due to the transition from electrons in the QW to the continuum of light-hole states in the barrier: E^1-$LH_{Barrier}$ and E^2-$LH_{Barrier}$. Despite a weaker wave-function overlap, these emission lines are stronger than the 1114-meV barrier emission because the electron population is orders of magnitude larger in the QW than the barriers.

The shoulder near 800 meV has its peak inside the high-energy tail of the main transition. Krispin *et al.* had previously identified two electron traps in GaNAs caused by split interstitial defects on single As sites: $(N\text{–}N)_{As}$ at E_v +800 meV and $(As\text{–}N)_{As}$ at E_v+1100 meV.[17] Thus, one explanation of the subband-gap emission is a radiative transition from the $(N\text{–}N)_{As}$ level. However, from new absorption and reliability data, it is more likely that it corresponds to the exciton peak. Nevertheless, these barrier defects could still be present, but the recombination might be primarily nonradiative.

Thermal linewidth broadening causes the gain and absorption spectra to peak a few meV higher than the true transition edge. The spontaneous emission spectrum peaks $\approx 0.2\text{–}0.5k_BT$ even higher than this due to the E^2 density of photon states prefactor.[18] Nevertheless, the transition edge can be accurately determined as the inflection point in any of these three spectra. Since the occupation probability is a maximum at the unbroadened transition edge, convolution with a symmetric line shape, e.g., Lorentzian, results in a maximal rate of increase at this edge.

Due to the band-gap reduction with temperature, the inflection point for the main QW peak redshifted; however, the shift was only 0.31 meV/K (0.41 nm/K) at 1 kA/cm^2 compared to the 0.34-meV/K (0.60 nm/K) redshift of the lasing wavelength. The inflection point shift decreased to 0.23 and 0.20 meV/K at 2 and 3 kA/cm^2, respectively. Band-gap renormalization (BGR) is strong in strained devices[19] and is responsible for these differences. At fixed current density, the carrier density of the E^1 and HH^1 levels decreases with temperature due to increased occupation of the higher levels and an increase in carrier leakage and/or Auger recombination. Thus, at fixed current density, the BGR is less at higher temperatures leading to an underestimate in the band-gap redshift with temperature; this measurement artifact becomes more pronounced at higher carrier densities, where BGR is stronger. The peak energy redshifted even less than the inflection point: 0.24, 0.20, and 0.17 meV/K at 1, 2, and 3 kA/cm^2, respectively. The E^2 density of photon states prefactor is probably responsible for this additional difference since the value of k_BT blueshifts by 0.086 meV/K.

The 942- and 1022-meV peak locations remained unchanged with temperature. Thermal broadening and increased emission on the high-energy side of these peaks from the E^1-$LH_{Barrier}$ and E^2-$LH_{Barrier}$ transitions, respectively, obscured any signs of the band-gap redshift.

The integrated QW emission rate decreased as expected due to the T^{-1} dependence of the radiative coefficient, B.[20] However, comparing the spectra at 50 and 90 °C of Fig. 2(b), the emission rate for the 942-, 1022-, and 1114-meV peaks increased with temperature because of the increase in occupancy of the higher QW levels and of thermionic emission of carriers from the QW into the barrier. Comparing 90 and 120 °C of Fig. 2(b), except for the 800-meV peak, there was a general rate decrease for all of the transitions, probably due to an increase in leakage or Auger recombination. With increasing temperature, the emission rate for the 800-meV peak appears to increase strongly and the emission energy appears to be unchanged. This is counterintuitive for the behavior of an exciton peak, but since the exciton peak moves rigidly with the band gap, which redshifts faster than the main QW TSE peak, the exciton peak emerges at high temperature. This led to an incorrect initial conclusion of increased emission at higher temperatures.

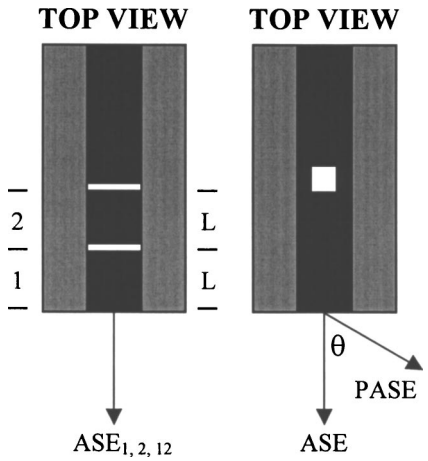

FIG. 3. Multisection gain measurement configuration on the left and (partial) amplified spontaneous emission with window configuration on the right.

MULTISECTION EXPERIMENTS

Measurement techniques

To study gain and obtain polarization-resolved spontaneous emission and absorption spectra, we applied an abbreviated version of the techniques of Thomson *et al.*[21] Two trenches, each 2 μm wide, were etched using a FIB through the top metal of a 1575-μm-long device with as-cleaved (R =30%) facets. The first two section lengths were 324 μm long each while the third was 927 μm long. On-axis amplified spontaneous emission (ASE) spectra were collected with a polarizer inserted between the collection and focusing lenses. The setup is shown in Fig. 3 along with the device section layout.

We omitted the angled facet after the unpumped section to be able to examine whether the FIB trenches affected laser performance. Above the absorption edge of the unpumped section ($\alpha > 12.0$ cm^{-1}), the collected ASE experiences a single-pass amplification because the round trip loss through the unpumped section is high: $R_R \exp(-2\alpha L_R) \ll 1$, where R_R=30% and L_R=927 μm. This approximation was validated by the lack of Fabry–Perot fringes at all measured currents. However, below the absorption edge, the internal loss of 7.5 cm^{-1} (presented later) might be insufficient to

fully attenuate the reflected light, especially at high injection currents (>1.5 kA/cm^2). The correction for subband-gap spectra due to multipass amplification is small for the absorption and emission measurements, but can reach 10% for the gain measurement. In future experiments, the absorbing region could be made longer and the facet reflectivity reduced while still keeping the mirror loss constant. This should preserve the threshold and efficiency values when all sections are probed, but improve the measurement accuracy at higher current densities. In addition, part of the absorbing region could be reverse biased to increase the subband-gap absorption due to the quantum-confined Stark effect (QCSE), which quadratically redshifts the band-edge transition energy as a function of the field. Care must be taken to ensure that the current injection of the pumped sections is not modified.

Electrical isolation of the sections is critical for high accuracy. The resistance between the metal contacts of the adjacent sections was measured to be 150 Ω. This is much greater than the 3–4 Ω device series resistance, so good electrical isolation was obtained. The effects of any current spreading are expected to be negligible since the carrier diffusion lengths are much smaller than the section lengths. Separate current sources were used to bias the sections rather than using two probes in parallel, because unequal contact resistances could lead to unequal current distribution between the sections.

Extreme care was taken during etching the metal at the edges of the ridge waveguide by decreasing the ion-beam strength and angling the beam at 45° to the metal surface, away from the ridge center, in order to minimize damage to the exposed parts of the AlGaAs *p*-cladding walls and GaAs waveguide underneath. The threshold and external efficiency with all three sections probed were only slightly degraded (4% and 7%, respectively) compared to devices without FIB trenches. It appears that the main effect of the FIB etch was to increase the waveguide scattering loss. The observed degradation of the threshold and efficiency is well accounted for if the internal loss is increased to 3.8 cm^{-1} from a value of 3.0 cm^{-1} obtained through a previous cavity length study[2] of the same wafer.

Polarization-resolved absorption, net gain, and TSE spectra were calculated, neglecting the subband-gap multipass correction, according to Ref. 21,

$$\alpha = -\frac{1}{L}\ln\left(\frac{\mathrm{ASE}_2}{\mathrm{ASE}_1}\right), \quad \Gamma g - \alpha_i = \frac{1}{L}\ln\left(\frac{\mathrm{ASE}_{12}}{\mathrm{ASE}_1} - 1\right),$$
$$\mathrm{TSE} \propto \frac{1}{L}\ln\left(\frac{\mathrm{ASE}_{12}}{\mathrm{ASE}_1} - 1\right)\frac{\mathrm{ASE}_1^2}{\mathrm{ASE}_{12} - 2\mathrm{ASE}_1}, \tag{1}$$

where ASE_1, ASE_2, and ASE_{12} are the ASE spectra when pumping section 1 only, section 2 only, and both sections, respectively, and L is the length of each section. The measurements were performed in cw mode to obtain a wider spectrum with high signal-to-noise ratio, but at the cost of device heating; $T_s = 15$ °C and T_a increased from T_s at low bias to 35 °C at 2 kA/cm^2.

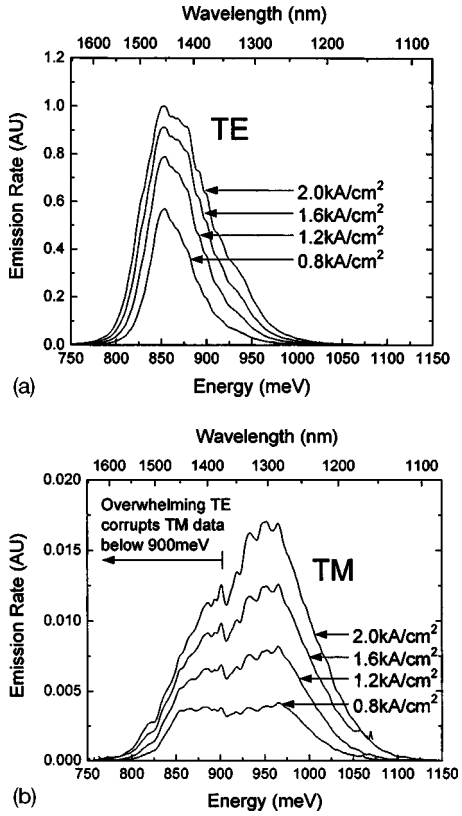

FIG. 4. (a), (b) Normalized TE and TM spontaneous emission spectra at $T_s = 15$ °C for 0.8, 1.2, 1.6, and 2.0 kA/cm^2. The TE peak is over 50× larger than the TM peak; below 900 meV, this ratio increases and the polarizer was unable to fully block the overwhelming TE signal. The ripples are an interference effect caused by beam clipping.

Spontaneous emission and gain results

Figures 4(a) and 4(b) show the normalized TE and TM TSE spectra at various current densities. From these spectra, we definitively identify two transitions located at 853 and 954 meV for 2 kA/cm^2 as *E*-HH and *E*-LH in nature. The two main peaks of the device used in Fig. 2(a) were at 865 and 940 meV for 2 kA/cm^2 ($T_a = 35$ °C). However, Fig. 4(b) shows that at 954 meV, the TM peak has only 10% of the amplitude of the TE spectrum in Fig. 4(a) and so the 940-meV peak must be mostly due to a TE transition. This transition is obscured by the high-energy tail of the 853-meV peak in Fig. 4(a).

Below the band-gap energy, the net gain spectrum asymptotes to the internal loss. We obtained a value for the internal loss of 7.5 ± 0.9 cm^{-1} for the TE mode. This value is slightly inconsistent with the estimate of 3.8 cm^{-1} based on how the threshold and efficiency for this device compared to the previous cavity length study. Below 900 meV, the ASE for the TM mode was so weak that the 1000:1 extinction ratio of the polarizer was insufficient to adequately suppress the overwhelming TE signal. As a result, the data were corrupted by the absorption signal of the TE mode, which pulled down the measured TM gain curve for the low-energy region. Thus, we cut the TM data below 900 meV, which prevented an accurate estimate of the internal loss for the TM mode. Nevertheless, extrapolating the TM gain spectrum to lower energies, we obtain an internal loss of the TM mode of 8 ± 3 cm^{-1}.

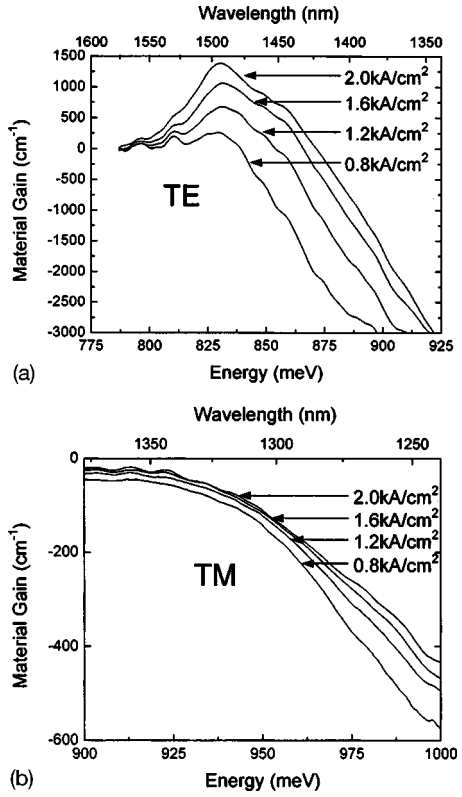

FIG. 5. (a), (b) Material gain spectra at $T_s=15\,^{\circ}\mathrm{C}$ for 0.8, 1.2, 1.6, and 2.0 kA/cm^2. The TE gain peak remains near 828 meV or 1500 nm rather than shifting to higher energies with current due to BGR and device heating. The TM spectra show absorptive loss at all measured currents due to the low occupancy of the light hole bands.

In calculating the material gain, which is plotted in Figs. 5(a) and 5(b) we assumed the same internal loss of 7.5 cm^{-1} for both modes and a confinement factor, Γ, of 1.4% for TE but 9.2% for TM since the light holes are spread throughout the barriers and QW due to the weak type-II alignment. The TE gain is peaked near 828 meV or 1500 nm. The peak is almost constant and does not shift to higher energies with current due to BGR and device heating. The TM spectra show absorptive loss at all measured currents due to the low occupancy of the light-hole bands. The peak TE material gain is plotted in Fig. 6. Above transparency, the fit for the

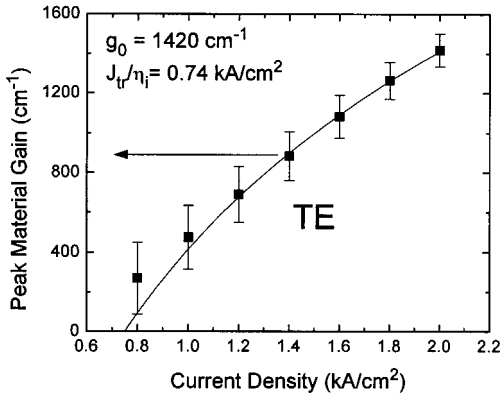

FIG. 6. Peak TE material gain vs current density. The logarithmic fit to the TE mode's *g-J* curve was $g=1420\,\mathrm{Ln}(J/0.74)$ where g is in cm^{-1} and J is in kA/cm^2.

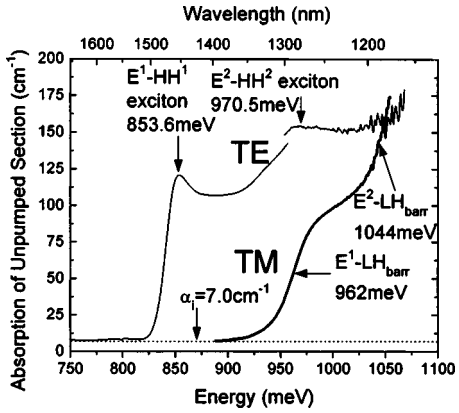

FIG. 7. Modal absorption spectra of the unpumped section for $T_a \approx T_s = 35\,^{\circ}\mathrm{C}$. Data were collected in two sweeps and joined at 1300 nm. The low-energy tail for both spectra asymptotes to the internal loss, $\alpha_i = 7.0$ cm^{-1}. The TE spectrum has exciton peaks for the E^1-HH^1 and E^2-HH^2 transitions at 853.6 and 970.5 meV, respectively. The TM spectrum has no visible exciton peaks. Transition energies for the E^1-LH$_{\mathrm{Barrier}}$ and E^2-LH$_{\mathrm{Barrier}}$ of 962 and 1044 meV were found using the inflection points.

TE peak gain to the empirical formula $g=g_0\ln(\eta_i J/J_{\mathrm{tr}})$, where g_0 is the gain coefficient, η_i is the internal quantum efficiency, and J_{tr} is the transparency current density, is good and we find $g_0=1420$ cm^{-1} and $J_{\mathrm{tr}}=0.37$ kA/cm^2. Both parameters are slightly different than the values of 1871 cm^{-1} and $J_{\mathrm{tr}}=0.48$ kA/cm^2 obtained through the pulsed mode cavity length study[2] because of device heating.

Absorption measurements

In the absorption measurement, the ASE of the second section served as an optical pump source for the unbiased first section.[21] Due to BGR with carrier density, the emission wavelength of the second section was redshifted and provided sufficient optical intensity for an absorption measurement well below the unpumped band gap. The modal absorption spectrum for the unpumped section for $T_a \approx T_s = 35\,^{\circ}\mathrm{C}$ is shown in Fig. 7. The strong wavelength dependence of the absorption and emission produced ASE spectra with over 40-dB amplitude contrast. To improve the measurement accuracy for the weaker part of the spectrum, overlapping spectra were taken with different OSA settings and the data were joined at 1300 nm (954 meV). The TM mode spectra, having a smaller amplitude contrast, overlapped cleanly, but the TE mode spectra showed a 6-cm^{-1} discontinuity, consistent with an OSA measurement error of 0.8 dB.

From the low-energy tail of Fig. 7, the internal loss was 7.0 cm^{-1} for both the TE and TM modes. Taking into account the multipass correction, the exact internal loss was slightly higher 7.6 ± 0.3 cm^{-1}. BGR pushed the main emission peak of the TE spectrum to a lower energy. As a fortuitous result, its distance to the unpumped TM absorption edge increased and the accidental collection of the overwhelming TE signal was significantly reduced. Without this systematic error, the internal loss for the TM mode was more accurately determined. Processes such as intervalence band absorption (IVBA) and free-carrier absorption (FCA) in the QW and barriers are absent since the section is unpumped and these regions are not intentionally doped. Thus, the in-

TABLE I. Energy-level separations and their method of determination for our GaInNAsSb SQW inside GaNAs barriers.

Index	Transition	Energy (meV)	Determination method
1	$(E^1-HH^1)^{Peak}_{Exciton}$	853.6±0.7	TE absorption exciton peak
2	$(E^2-HH^2)^{Peak}_{Exciton}$	970.5±1.8	TE absorption exciton peak
3	$(E^2-E^1)+(HH^1-HH^2)$	117±2	(2) minus (1)
4	$E^1-LH_{Barrier}$	962±2	TM absorption inflection point
5	$E^2-LH_{Barrier}$	1044±4	TM absorption inflection point
6	E^2-E^1	82±4	(5) minus (4)
7	HH^1-HH^2	35±5	(3) minus (6)
8	$E_g^{Barrier}=(E-LH)_{Barrier}$	1094±5	TSE inflection point
9	$E_{Barrier}-E^1$	132±5	(8) minus (4)
10	$(E-HH)^{Peak}_{Barrier}$	1158±10	TSE peak
11	$(E-LH)^{Peak}_{Barrier}$	1114±8	TSE peak
12	$(LH-HH)_{Barrier}$	44±13	(10) minus (11)
13	$(LH-HH)_{Barrier}$	42	Theory-Vegard's law
14	$(E-HH)_{Barrier}$	1138±14	(8) plus (12)
15	$(E^1-HH^1)_{Exciton}$	843±3	TE absorption inflection point
16	$E_b^{Exciton}$	16±5	Theory
17	E^1-HH^1	859±6	(15) plus (16)
18	E^2-HH^2	976±6	(3) plus (17)
19	$HH^1-LH_{Barrier}$	103±6	(4) minus (17)
20	$HH^1-HH_{Barrier}$	147±14	(12) plus (19)
21	$(HH-LH)_{QW}$	131	Theory-Vegard's law

ternal loss of 7.6 cm^{-1} represents the waveguide scattering loss and absorptive loss of the doped cladding layers; the actual internal loss may be higher during laser operation.

Band structure

Band offsets, band gaps, and effective masses can be calculated through measurements of the inflection points in the absorption and TSE spectra. In some cases, greater accuracy was achieved using the energy difference between peak locations. The determination method of various energy levels and their uncertainties are described in Table I. The TE absorption has an exciton peak for the E^1-HH^1 transition at 853.6 meV with a full width at half maximum (FWHM) of 14.3 meV and a faint exciton peak for the E^2-HH^2 transition at 970.5 meV. For the finite QW with 7.8-nm thickness, the exciton binding energy is estimated to be significant: $E_b^{Exciton} \approx 16$ meV due to the large predicted effective mass in the band anticrossing model.[22] No exciton peak is visible for the E^1-HH^3 transition because the transition is only weakly allowed and may be obscured by the absorption edge of the E^1-$LH_{Barrier}$ transition. The TM absorption spectrum has no visible exciton peaks because the light-hole exciton reduced mass is 50% smaller and the light holes are unconfined and therefore form more of a 3D-like exciton. Both differences lead to a smaller exciton binding energy. The peak would be easily smeared into the main band to band transition.

From high sensitivity TSE data, we were able to observe an extremely weak peak at 1158 meV beyond the 1114-meV peak described in Fig. 2. We believe these correspond to the $(E\text{-}HH)_{Barrier}$ and $(E\text{-}LH)_{Barrier}$ transitions, respectively. Since the carrier density is small in the barriers, we can assume negligible BGR for the barriers and consider them unpumped. Also, due to the proximity of the two transitions, we can assume that the TSE peaks are the same distance from their respective transition edge. Thus, we obtain the strain-induced valence-band splitting, $(LH\text{-}HH)_{Barrier}$, of 44 meV. Using a linear interpolation (Vegard's law) for the deformation potentials and lattice constants of zinc-blende GaN (Ref. 11) and GaAs,[15] we calculate a strain-induced splitting of 42 meV for $(HH\text{-}LH)_{Barrier}$, which agrees quite well with the measured value. There have been reports (at 80 K) of enhanced valence-band splitting in GaNAs/GaAs (Refs. 23 and 24) attributed to nonlinear behavior in the deformation potential *b*. However, at room temperature, the measured valence-band splitting of ≈42 meV for 2.3% nitrogen in Ref. 23 is consistent with our results and interpolation. Lacking any reports in the literature for the quinary GaInNAsSb QW, we can only give a rough estimate for the $(HH\text{-}LH)_{QW}$ strain splitting of 131 meV using a linear interpolation of the data for the six binary alloys: GaAs, GaN, GaSb, InAs, InN, and InSb found in Refs. 11 and 15.

With various level separations experimentally determined, specifically $E_{Barrier}$-E^1, E^2-E^1, E^1-HH^1, HH^1-HH^2, and HH^1-$HH_{Barrier}$ (Refs. 9, 6, 17, 7, and 20 of Table I), we minimized the weighted least-squares fit to finite quantum well theory. The QCSE due to the built-in field of 35 kV/cm produces less than a 2-meV shift for any of the energy levels. This is small compared to the measurement error and so the QCSE was neglected in these calculations. The barrier effective masses were taken to be $m_e^{Barrier}=0.072m_0$ (Ref. 25) and $m_{hh}^{Barrier}=0.355m_0$ using linear interpolation for the Luttinger parameters in Ref. 11. The quantum well thickness was $L_z=7.8$ nm. The adjustable parameters apply to the QW and were the band gap E_g^{QW}, the effective masses m_e^{QW} and m_{hh}^{QW}, and the conduction-band offset ratio Q_c^{QW}. The four parameter fit may be rearranged into four nonlinear coupled equations that can be solved exactly as follows: given $m_e^{Barrier}$,

TABLE II. Derived band diagram parameters and their method of determination. Note that all values include strain effects.

Index	Parameter (units)	Value	Determination method
22	$m_e^{\text{Barrier}}(m_0)$	0.072±0.030	Ref. 25
23	$m_{\text{hh}}^{\text{Barrier}}(m_0)$	0.355±0.030	Ref. 11-Vegard's Law
24	L_z(nm)	7.8±0.5	HR-XRD
25	Q_c^{QW}(%)	50.8±2.1	Least-squares fit–free parameter
26	E_g^{QW}(meV)	815±7	Least-squares fit–free parameter
27	$m_e^{\text{QW}}(m_0)$	0.113±0.024	Least-squares fit–free parameter
28	$m_{\text{hh}}^{\text{QW}}(m_0)$	0.35±0.09	Least-squares fit–free parameter
29	E^1-E_c(meV)	32±2	Least-squares fit
30	E^2-E_c(meV)	114±6	Least-squares fit
31	E_v-HH^1(meV)	12±2	Least-squares fit
32	E_v-HH^2(meV)	47±7	Least-squares fit
33	E_v-HH^3(meV)	102±14	Least-squares fit
34	E_v-HH^4(meV)	158±12	Least-squares fit
35	ΔE_c(meV)	164±5	Multiple: e.g., (9) plus (29)
36	ΔE_v^{HH}(meV)	159±12	Multiple: e.g., (20) plus (31)
37	$\Delta E_v^{\text{Effective}}$(meV)	115±6	Multiple: e.g., (19) plus (31)
38	E_g^{GaAs}(meV)	1424	Ref. 15
39	$Q_c^{\text{GaNAs/GaAs}}$(%)	74±5	Ref. 25
40	$\Delta E_c^{\text{GaNAs/GaAs}}$(meV)	244±17	(8), (38), and (39)
41	$m_{\text{so}}^{\text{QW}}(m_0)$	0.12	Refs. 11 and 15-Vegard's Law
42	$\Delta_{\text{so}}^{\text{QW}}$(meV)	360	Refs. 11 and 15-Vegard's Law
43	$E_{\text{Trap}}^{(\text{N-N})_{\text{As}}} - E_v^{\text{GaNAs}}$(meV)	830	Ref. 17 and $Z_0 \approx 1.3$
44	$E_{\text{Trap}}^{(\text{As-N})_{\text{As}}} - E_v^{\text{GaNAs}}$(meV)	1100	Ref. 17

$m_{\text{hh}}^{\text{Barrier}}$, and L_z, there are unique solutions for (a) m_e^{QW} given $\text{E}_{\text{Barrier}}$-$\text{E}^1$ and E^2-E^1 and for (b) $m_{\text{hh}}^{\text{QW}}$ given HH^1-$\text{HH}_{\text{Barrier}}$ and HH^1-HH^2. E_g^{QW} is determined using E^1-HH^1 and the confinement energies calculated while solving (a) and (b). Finally, Q_c is obtained using the confinement energies and $\text{E}_{\text{Barrier}}$-$\text{E}^1$ and HH^1-$\text{HH}_{\text{Barrier}}$. Thus, each parameter can be obtained analytically with high accuracy; however, the least-squares fit is preferable, especially if additional level separation data exist, e.g., HH^1-HH^3, or if the data are to be weighted according to measurement uncertainty.

Table II summarizes the free and derived fit parameters. From the fit, we find $Q_c^{\text{QW}}=50.8\pm2.1\%$, $E_g^{\text{QW}}=815\pm7$ meV, $m_e^{\text{QW}}=0.113\pm0.024m_0$, $m_{\text{hh}}^{\text{QW}}=0.35\pm0.09m_0$, $\Delta E_c=164\pm5$ meV, and $\Delta E_v^{\text{HH}}=159\pm12$ meV. All of these parameters include the effects of strain and would be significantly different for lattice-matched material. With the barrier heights and effective masses, the flatband thermionic emission lifetimes[26] for electrons and heavy holes into the barriers are 28 and 40 ps, respectively. However, the effective valence-band barrier height, $\Delta E_v^{\text{Effective}}$, is only 115±6 meV because of the light holes. With the smaller effective barrier height, the thermionic emission lifetimes for holes could be less than 7 ps if there is efficient scattering from the heavy- to light-hole bands at the QW interfaces. Also, assuming that the estimated $(\text{HH-LH})_{\text{QW}}$ strain splitting of 131 meV is correct, then the LH is unconfined in the QW and is type II by 16 meV. At elevated temperatures or currents, there will be a significant concentration of holes in the barriers. The fit predicts two electron and three heavy-hole levels with confinement energies of 32 and 114 meV for electrons and 12, 47, and 102 meV for heavy holes and that there might be a fourth heavy-hole level about 1 meV from the heavy-hole barrier. This possible level will be ignored because of its weak confinement and proximity in energy to the barrier. It is already deep within the continuum of light-hole barrier states.

Aside from uncertainty in the measured level separations, errors in the quantum well thickness and barrier effective masses are the main sources of uncertainty in the fit parameters. All three uncertainties were included in calculating the error estimates of the fit and derived parameters. The latter two primarily affect the effective masses while the former obviously affects all parameters. Some of the derived parameters, most notably the band offsets, can be calculated from the data and fit parameters in multiple ways; using the level separation data and calculated confinement energies instead of (or in addition to) Q_c and the band gaps can significantly reduce their uncertainties. The overall accuracy of the absorption/TSE technique can be significantly improved by performing a quantum well thickness study using GaAs barriers, whose parameters are more accurately known.

The flatband diagram at $T_a=35$ °C for our annealed 7.8-nm $\text{Ga}_{0.62}\text{In}_{0.38}\text{N}_{0.023}\text{As}_{0.950}\text{Sb}_{0.027}$ SQW inside 22-nm $\text{GaN}_{0.025}\text{As}_{0.975}$ barriers embedded in a GaAs waveguide is shown in Fig. 8. Energies, in units of meV, are relative to the quantum well heavy-hole valence-band maximum. The offsets for GaNAs to GaAs of $\Delta E_c=244$ meV and $\Delta E_v^{\text{LH}}=86$ meV were approximated using the formulas in Ref. 25 to calculate $Q_c^{\text{Barrier}}=74\%$, but using our data for $(\text{E-LH})_{\text{Barrier}}=1094$ meV which is blueshifted by 68 meV compared to Ref. 25, presumably due to differences in growth and because our sample was annealed.

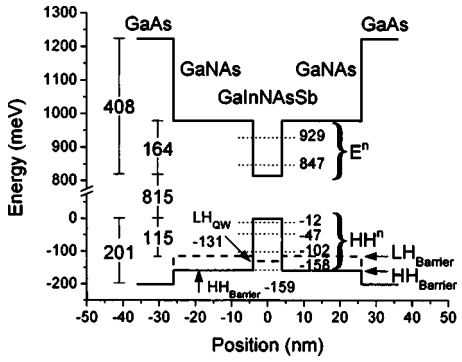

FIG. 8. Flatband diagram with confinement energies for our 800 °C annealed, unpumped, 7.8-nm $Ga_{0.62}In_{0.38}N_{0.023}As_{0.950}Sb_{0.027}$ SQW inside 22-nm $GaN_{0.025}As_{0.975}$ barriers embedded in a GaAs waveguide at $T_a = 35$ °C. Energies, in units of meV, are relative to the HH QW valence-band maximum. The QW is type I for the HH band, but type II for the LH band. There are two electron and three HH confined levels. A fourth, weakly confined, HH level is 1 meV from the HH barrier.

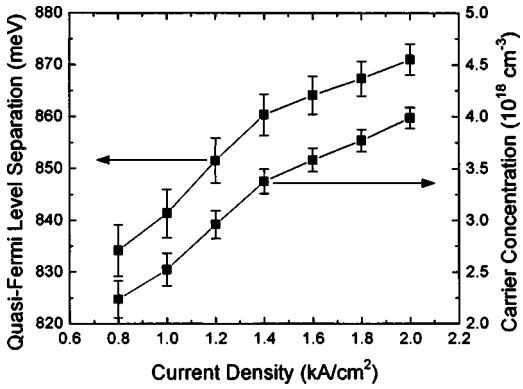

FIG. 9. Quasi-Fermi-level separation (upper curve) and carrier concentration (lower curve) vs current density. The lines serve as guides for the eyes.

The GaInNAsSb band gap, offsets, and effective masses obtained here show excellent agreement with photoreflectance (PR) measurements of an unannealed sample grown under the same conditions[27] after accounting for the annealing blueshift. Photoreflectance determined $E_g^{QW} = 783$ meV, $m_e = 0.12m_0$, $\Delta E_c = 144$ meV, and $\Delta E_v^{HH} = 127$ meV at room temperature. Comparing the two measurements, the QW and barrier band gaps are blueshifted by 32 and 84 meV, respectively. Given the measurement uncertainty and separate growths, it is unclear whether the barrier heights increase with annealing.

Absorption measurements were also made for $T_a \approx T_s = 15$ and 65 °C. Other than a miniscule decrease in the exciton absorption strength, all of the features in the TE and TM absorption curves overlap exactly when the spectra are redshifted by 0.36 meV/K. Since BGR is nonexistent in the unpumped section, we conclude that 0.36 meV/K is the true value for the band-gap redshift with temperature.

Band-gap renormalization

By comparing the TSE and gain spectra inflection points in Figs. 4(a) and 5(a) of 824±3 and 822±4 meV to the unpumped E^1-HH^1 transition energy of 859±6 eV, we find a band-gap renormalization of 36±7 meV for $J = 2.0$ kA/cm^2 and $T_a = 35$ °C. BGR is a substantial effect responsible for redshifting the lasing wavelength over 60 nm. Unfortunately, this implies that as the threshold carrier density is reduced through growth and processing improvements, the GaInNAs(Sb) compositions will need to be readjusted and growth conditions reoptimized to maintain long wavelength operation.

From the zero crossing of the material gain curves in Fig. 5(a), we determined the quasi-Fermi-level separation for current densities above transparency, shown as the upper curve in Fig. 9. At 2.0 kA/cm^2, the quasi-Fermi-level separation was 871 meV. Thus, the carrier density was $n = 3.99 \times 10^{18}$ cm^{-3} or $n_{surface} = 3.11 \times 10^{12}$ cm^{-2}, using the inflection data for E^1-$HH^1 = 823$ meV. BGR scales roughly as $cn_{surface}^{1/3}$ for a QW structure, where c is a constant of proportionality. Thus, $c = 25$ meV/$(10^{12}$ cm$^{-2})^{1/3}$ which is slightly smaller than the values given in Ref. 28 for a GaAs/AlGaAs QW. With all three sections pumped, the device lased at $J_{th} = 1.6$ kA/cm^2 ($n_{th} \approx 3.6 \times 10^{18}$ cm^{-3}) and $T_a = 35$ °C; thus, we calculate 35±7-meV band-gap renormalization at threshold. We were unsuccessful in using the crossing of the TE and TM net modal gain curves to verify the quasi-Fermi-level separations as described in Ref. 21. As mentioned previously, the slight presence of the TE signal was enough to affect the TM curve for energies below 900 meV.

Carrier density

Invoking charge neutrality, neglecting the QCSE, accounting for device heating and BGR, and using the band structure of Fig. 8 and measured quasi-Fermi-level separations, we calculated the dependence of carrier concentration on applied current density in the lower curve of Fig. 9. Typically, BGR is neglected and the band gap is assumed to be constant and equal to the lasing energy for all biases when calculating the carrier concentration versus current using quasi-Fermi-level separation data. However, the increase in renormalization from transparency to 2.0 kA/cm^2 is almost 20% as large as the increase in quasi-Fermi-level separation. Neglecting BGR leads to a 10% overestimate of the carrier concentrations at transparency. Even when BGR is included there still remain some uncertainties in the *n*-*J* curve because the exact distribution of the BGR energy is difficult to calculate. For simplicity, we assumed a 50/50 split of the BGR energy between conduction and valence bands and that each confined level experiences an equal renormalization.

The material gain is plotted versus carrier density in Fig. 10. The gain fits well to a linear relationship having a differential gain of $dg/dn = 7.3 \times 10^{-16}$ cm^2 and a transparency of $n_{tr} = 2.08 \times 10^{18}$ cm^{-3}. A logarithmic relationship also works well for the *g*-*n* curve due to the limited range of measured carrier densities. The fitted transparency carrier concentration agrees excellently with a band-structure calculation of $n_{tr} = 2.09 \times 10^{18}$ cm^{-3} for $T_a = 20$ °C. However, the differential gain is significantly less than the value of 1.2×10^{-15} cm^2 at $T_a \approx 20$ °C for a 10×750 μm^2 HR/cleaved device from the same wafer reported in Ref. 29 obtained through a relative intensity noise measurement. We attribute the discrepancy to wafer uniformity and device heating. The other laser was inherently better, possessing a 20% lower

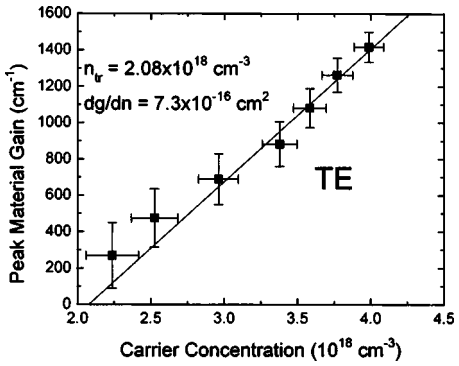

FIG. 10. Peak TE gain vs carrier concentration and its linear fit. The differential gain was $7.3\times10^{-16}\,\mathrm{cm}^2$ and the transparency concentration was $2.08\times10^{18}\,\mathrm{cm}^{-3}$.

threshold for the same T_a. Also, the differential gain measured from Fig. 10 is significantly underestimated due to device heating. The transparency concentration increases and the differential gain decreases with temperature, leading to a sharp reduction in gain at fixed carrier concentration. Applying the gain formulas in Ref. 30 to our band structure, we calculate that the measured differential gain would have been 8.9×10^{-16} cm^2 if T_a were held constant at 20 °C instead of increasing from 20 °C at transparency to 35 °C at 4×10^{18} cm^{-3}.

INTERNAL EFFICIENCY AND PINNING OF TSE

In pulsed mode, $T_s=15$ °C, the TSE-EDGE spectra were collected for various current densities for a 20×533 μm^2 device. Lasing occurred at 851 meV and 1.7 kA/cm^2. The lasing energy is blueshifted compared to previous data due to the lower T_a in pulsed mode. The emission rate at evenly spaced energies was extracted and a few are plotted versus the current in Figs. 11(a) and 11(b). The vertical axis in Fig. 11(b) is one-fifth that of Fig. 11(a). In both figures, the spontaneous emission rate for each of the energies continued to increase above threshold. The increase in the 851-meV curve at threshold is due to scattered laser light.

Above threshold, the Fermi levels and carrier concentrations are expected to pin strongly because stimulated emission should consume every additional injected carrier.[31] The spontaneous emission should saturate for wavelengths close to lasing wavelength. However, Fig. 11(a) shows that the spontaneous emission is only weakly clamped. For energies near 851 meV, but outside the lasing spectrum (not shown in Fig. 11), the emission efficiency (slope) above threshold is still about 22% of the below threshold value, indicating that the carrier concentrations are not pinned throughout the entire structure. The emission efficiency ratio was also 22% near the 940-meV TSE peak (E^1-HH^3,E^1-$LH_{Barrier}$), but it increased to 34% near the 1022-meV TSE peak (E^2-HH^2,E^2-$LH_{Barrier}$), and was close to 100% near the 1114-meV peak (E-LH)$_{Barrier}$. If carriers do not rapidly scatter from excited bands, less pinning would be expected for transitions not involving the main levels E^1 and HH^1.

Partially amplified spontaneous emission (PASE) spectra in the QW plane at $\theta=50°$ relative to the optical axis were also collected. We call it PASE because spontaneous emission emitted at an angle of 12° relative to the optical axis can traverse as much as 100 μm inside the 20-μm wide device and still be collected, and in addition some on-axis ASE might be scattered into the collection assembly. Nevertheless, PASE primarily consists of the unamplified spontaneous emission at the facet. As a result, the PASE peak wavelength and other spectral features are between that of the TSE and ASE. The emission efficiency ratio was 16% near 851 meV and 14% near 940 meV, but ratios for the other peaks could not be computed because of insufficient signal strength in pulsed mode.

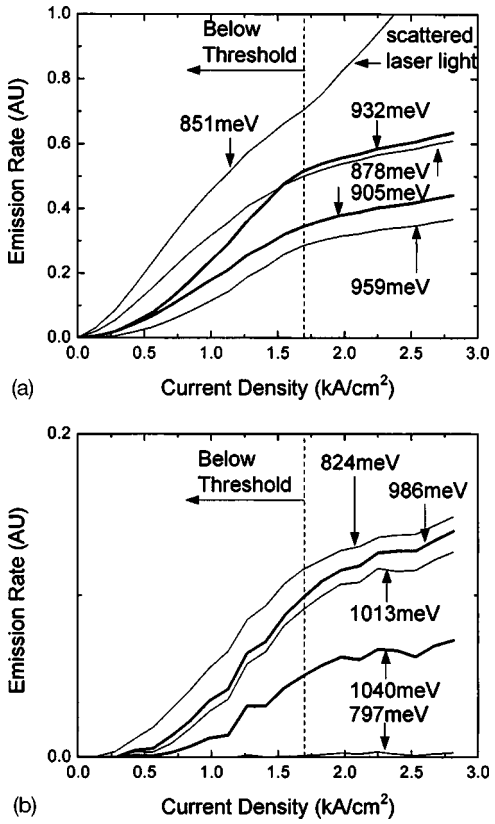

FIG. 11. TSE-EDGE spectra at 15 °C at uniformly spaced energies vs current density in pulsed mode. Lasing occurred for this 20×533 μm^2 device at 851 meV and 1.7 kA/cm^2. (a) has this scattered laser emission plus four other emission energies, while (b) is a zoomed view of the five weaker emission energies. Above threshold, emission from the energies close to the lasing transition is only weakly clamped. The clamping is even weaker for transitions not involving the main levels E^1 and HH^1.

The optics in the EDGE configuration primarily image the section of the active region near the ridge-waveguide edge where lateral current/carrier spreading provide fewer carriers and the optical field is weaker than in the direct center of the ridge. There would be lower gain and weaker stimulated emission at the edge and this could explain the continued spontaneous emission above threshold. Since the optics in the PASE spectra image an entire waveguide cross section, whose emission is dominated by the ridge center, the PASE spectra should clamp more strongly than the EDGE spectra, which it did, 16% vs 22%. Another carrier spreading effect is nonuniform injection along the cavity length because the top metal contact was only 2000 Å thick. This longitudinal nonuniformity was partially alleviated by probing the sample every 250 μm along the length.

These two nonuniform spreading effects would reduce the device's quantum efficiency by η_s^d, the current spreading efficiency factor, described in Refs. 31 and 32. From the PASE measurement, we calculate $(\eta_s^d)_{\text{lateral}}=84\%$ for lateral spreading. For longitudinal spreading, we measured the external differential quantum efficiency and threshold with various probe separations. The values improved as the probe separation was reduced, but the improvements saturated for separations less than 400 μm. Thus, $(\eta_s^d)_{\text{longitudinal}}\approx 100\%$ for our experiments. Therefore, nonuniform spreading only partially explains the device's low internal efficiency of 45%–55%.

Another explanation of the low efficiency and its temperature dependence is poor injection efficiency, η_i^d also described in Refs. 31 and 32. We suspect that carriers, even those near the ridge center, can continue to recombine nonradiatively above threshold through traps in the barriers because the barrier populations do not clamp strongly at threshold.[33] The $(\text{N–N})_{\text{As}}$ and $(\text{As–N})_{\text{As}}$ split interstitial defects are formed during barrier growth as a means to partially compensate tensile strain.[17] Provided that the traps are accessible to electrons, the trap recombination rate will be limited by hole capture, which is proportional to the density of holes in the barrier. Thus, recombination in the *p*-side barrier should be larger than in the *n*-side barrier. Electrons can reach *p*-side barrier traps in three ways: traversing the QW during injection, tunneling from the QW to defects near the QW/barrier interface, or after thermionic emission from the QW into the barriers. The $(\text{As–N})_{\text{As}}$ defect easily captures electrons during injection since it is at the same energy as the GaNAs barrier conduction-band minimum. This direct capture process obviously reduces η_i^d. The $(\text{N–N})_{\text{As}}$ defect is located $\approx$100 meV below the QW conduction-band edge and so capture after thermionic emission is more likely for this trap, especially at elevated temperatures or carrier densities. Phonon-assisted tunneling from the QW to the $(\text{N–N})_{\text{As}}$ trap becomes easier as the electron levels of the QW become more resonant with the defect level at high temperatures or carrier densities due to band-gap redshifting and BGR, respectively. The presence of these traps and their effect on threshold current density will be explored subsequently through *Z*-parameter measurements.

LOCAL *Z* PARAMETER

Theory

Analysis of radiative and nonradiative recombination can be made by measurements of the local *Z* parameter. The *Z* parameter describes the dominant process for recombination in semiconductor lasers.[34,7,8] The injected current balances the net recombination in steady state. Assuming Boltzmann statistics, charge neutrality $n=p$ in the undoped QW, and neglecting stimulated emission, this balance is expressed according to

$$I_{\text{Tot}} = eV_aR(n), \quad R(n) = An + Bn^2 + Cn^3, \tag{2}$$

where I_{Tot} is the total current, e is the electronic charge, V_a is the active volume, $R(n)$ is the net recombination rate, and A, B, and C are the monomolecular, radiative, and Auger coefficients, respectively. The total spontaneous emission rate is proportional to the radiative current, I_{Rad},

$$I_{\text{Rad}} = eV_aBn^2, \quad \text{TSE} \propto I_{\text{Rad}} \propto n^2. \tag{3}$$

If one of the recombination processes dominates the current, Eq. (2) can be approximated by,

$$I \propto n^Z, \tag{4}$$

where Z can range from 1 to 3 if the current is dominated by monomolecular ($Z\approx 1$), radiative ($Z\approx 2$) or Auger recombination ($Z\approx 3$). This interpretation is valid for a limited current range. From Eqs. (3) and (4), Z can be solved for as the derivative of the $\ln(I)$ vs $\ln(\text{TSE}^{1/2})$ relationship. Defining the local Z parameter as this instantaneous derivative, and assuming A, B and C are independent of n, Eqs. (2) and (3) yield[35]

$$Z \equiv \frac{d[\ln(I)]}{d[\ln(\text{TSE}^{1/2})]} = 1\frac{I_{\text{Mono}}}{I_{\text{Tot}}} + 2\frac{I_{\text{Rad}}}{I_{\text{Tot}}} + 3\frac{I_{\text{Aug}}}{I_{\text{Tot}}}, \tag{5}$$

where I_{Mono} and I_{Aug} are the monomolecular and Auger currents. This extends the previous interpretation of Z to range continuously as an average of the Z parameters for the various processes weighted by their fractional contribution to the total current. Z is bounded between 1 and 3 where monomolecular and Auger dominate. Any departure from $Z=2$ indicates the presence of nonradiative recombination, but $Z=2$ can also occur with equal amounts of monomolecular and Auger recombination since Z can be reexpressed as

$$Z = 2 + \frac{I_{\text{Aug}} - I_{\text{Mono}}}{I_{\text{Tot}}} \tag{6}$$

by using $I_{\text{Rad}}=I_{\text{Tot}}-I_{\text{Aug}}-I_{\text{Mono}}$. A value of Z below 1.5 indicates that at least 50% of the current is monomolecular.

In real devices, two nonideal effects complicate the *Z*-parameter analysis. First, there can be significant carrier leakage into the barriers or separate confinement heterostructure (SCH) waveguide at high injection levels. Using the band-structure data of Fig. 8 and assuming parabolic bands, we calculate that the electron and hole barrier populations increase superlinearly with the quantum well carrier density as n^{r}. For electrons, this exponent r increases from 1.0 to 2.1 as n increases from zero to $2.5N_c$, where $N_c=1.6\times 10^{18}\ \text{cm}^{-3}$ is the effective conduction-band density of states. For holes, it only increases from 1.0 to 1.2 over the same carrier densities. The exponent r increases more rapidly when the band is degenerate and is about 3% larger in the SCH waveguide due to the increased barrier height. Therefore, carrier leakage can vary anywhere from n^1 to $n^{2.1}$ for monomolecular barrier recombination, n^2 to $n^{3.3}$ for radiative barrier recombination, n^1 to $n^{2.2}$ for diffusive leakage into the SCH cladding, and n^2 to $n^{5.2}$ for drift leakage. Thus, $Z>3$ would seem to be good evidence of carrier leakage. Drift leakage is proportional to the SCH carrier density and also the injected current[36] so the exponent can be much larger and vary more depending on whether the injected current is dominated by monomolecular, radiative, or Auger recombination. However, drift and diffusive leakage into the SCH cladding were calculated to be negligible in our devices[33]

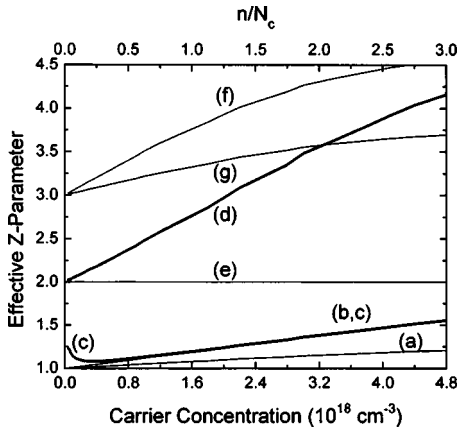

FIG. 12. Simulation of the behavior of the Z parameter vs carrier density for the band structure of Fig. 8 for cases where the current is dominated by a particular recombination mechanism: (a) midlevel QW traps, (b) midlevel barrier traps, (c) $(N–N)_{As}$ barrier electron traps, (d) $(As–N)_{As}$ barrier electron traps, (e) radiative, (f) Auger *CHCC*, and (g) Auger *CHHS*. Curves (a) and (b) begin together but separate since the barrier population increases superlinearly. Incomplete trap filling in curve (c) can cause $Z_0>1$ and Z to initially decrease. As the traps fill, curve (c) asymptotes to (b). Curve (e) has a constant value of 2.

because of the high electrical conductivity in the AlGaAs cladding layers and large AlGaAs/GaAs heterobarriers.[37] Further, the TSE measurements of Figs. 2(a) and 2(b) show that radiative barrier recombination is negligible. Auger recombination in the barriers is also negligible due to the lower carrier concentrations and larger band gap.

Second, and more importantly, Fermi–Dirac statistics must be used for the high injection levels encountered during typical laser operation. Assuming that electrons become degenerate first ($m_{hh}>m_e$) the electron Fermi occupation factor of the ground state, f_e^{GS}, asymptotes to unity while the hole occupation factor, f_h^{GS}, remains proportional to p. In this degenerate limit, the radiative rate for the E^1-HH^1 transition is no longer proportional to n^2, but rather asymptotes to being proportional to n. By the same argument, the dominant channel for *CHCC* (C=conduction, H=heavy hole) Auger recombination will asymptote to being proportional to n, while *CHHS* (S=split-off) recombination will asymptote to n^2.[38] However, the number of carriers capable of satisfying both energy and momentum conservation for these Auger processes increases superlinearly. Numerically integrating the formulas in Ref. 39, we find that *CHCC* increases from n^3 to $n^{3.8}$ and *CHHS* increases from n^3 to $n^{3.1}$ as n increases from zero to $2.5N_c$. Thus, Z will exceed 3 for both *CHCC* and *CHHS* processes. The dependence of Auger recombination on carrier density is quite sensitive to the band gap, effective masses, and whether the process is phonon assisted.[40] Z will remain constant at 2 for radiative recombination, but increase from 1 to 2 for monomolecular recombination in the QW and will be larger for monomolecular barrier recombination. Although the first electron band becomes degenerate, the second band, 82 meV higher, remains nondegenerate and so these degeneracy effects are less pronounced here than in the case of a QW with only 1 confined electron and hole level.

Figure 12 is a simulation of the behavior of the Z parameter (using its logarithmic derivative definition) versus carrier density at 35 °C if the current is completely dominated by various recombination mechanisms that might exist in our device: (a) midlevel QW traps, i.e., ideal monomolecular, (b) midlevel barrier traps, (c) $(N–N)_{As}$ barrier electron traps, (d) $(As–N)_{As}$ barrier electron traps, (e) radiative, (f) Auger *CHCC*, and (g) Auger *CHHS*. Some additional parameters used in the simulation were listed at the end of Table II. Z increases for processes (a)–(d) because of degeneracy and for (f) and (g) because of the increase of carriers that can conserve energy and momentum. A quick calculation shows that the second half of Eq. (5) can be generalized to the degenerate regime and to handle carrier leakage and other recombination processes simply by replacing the weighting coefficients, at each carrier density, with the effective Z values given in Fig. 12,

$$Z=\sum_{\text{AllProcesses}} Z_{\text{Effective}}\frac{I_{\text{Process}}}{I_{\text{Tot}}}. \tag{7}$$

Due to the small density-of-states ratio $\mu=N_c/N_v=m_e/m_{hh}=0.32$, the conduction band quickly becomes degenerate at low injection levels. The electron quasi-Fermi level crosses the first confined electron level at $n=1.2\times10^{18}$ cm^{-3} ($n/N_c=0.75$ or $J\approx0.4$ kA/cm^2). Above that point, Eq. (7) should be used instead of (5) and (6).

Experiment

To measure the Z parameter at various currents and temperatures in a reasonable amount of time, the integrated TSE was measured with an InGaAs *p-i-n* detector instead of collecting the spectra with the OSA and integrating numerically. Since the integrated TSE rate is the desired quantity, the InGaAs detector will perform the integration electrically provided that the detector's quantum efficiency is independent of wavelength. The detector used had a quantum efficiency that was flat to within 6% over the 300-nm range of the two dominant emission peaks of Figs. 2(a) and 2(b) and so the overall accuracy was only slightly deteriorated using this shortcut.

The WINDOW configuration in cw mode, with 1-mA current steps, was used on a 10×750 μm^2 HR/cleaved device ($J_{th}^{cw}=1.1$ kA/cm^2 at $T_s=15$ °C) to obtain the local Z parameter at various temperatures. The data, plotted in Fig. 13(a), were collected in cw mode to improve the accuracy of the applied current. The device failed suddenly during the $T_s=65$ °C measurement, indicated by the abrupt drop of Z. At low current density but above J_{Trap} (to be discussed later), the Z parameter appears to be independent of temperature and increases almost linearly with current density. At threshold, the TSE weakly clamps and the Z parameter diverges to $+\infty$. The sudden rise in Z provides a surprisingly good indicator of lasing threshold. At room temperature, $T_s=25$ °C, Z increases gradually from 1.2 to above 2.0 just below threshold. At low currents, the device is clearly dominated by monomolecular recombination. Near threshold, Z is rising and $Z_{th}\approx2$ indicating comparable and sizable amounts of monomolecular and leakage or Auger recombination. A possible distribution of the threshold current at room temperature, which is consistent with Eqs. (5) and (6), is 40% mono-

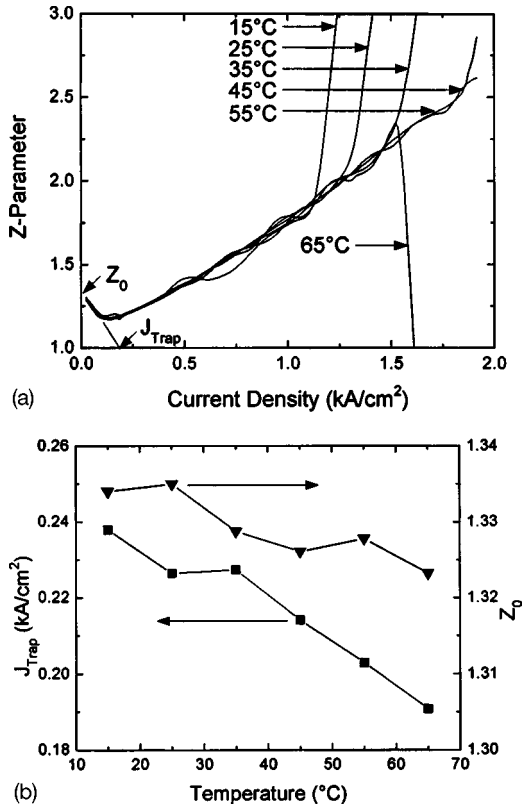

FIG. 13. (a) is the measured Z parameter for $T_s=15$–$65\,^{\circ}\mathrm{C}$ vs current density for $10\times750\ \mu\mathrm{m}^2$ device using WINDOW configuration in cw mode ($J_{\mathrm{th}}^{\mathrm{cw}}=1.0\ \mathrm{kA/cm^2}$ at $T_s=15\,^{\circ}\mathrm{C}$). The kink in the Z-J curve is also a good indicator of threshold. (b) is J_{Trap} and Z_0 vs stage temperature. The lines serve as a guide for the eyes in (b).

molecular, 20% radiative, and 40% Auger. However, due to high injection at threshold and possible leakage, a 70% barrier and QW trap recombination, 20% radiative, and 10% Auger distribution is more consistent with our band-structure measurements and Eq. (7). This device has a thermal resistance of 45 K/W. In cw mode, this produces a slight temperature rise in T_a of 6–13 °C when the threshold increases from 1 to 2 $\mathrm{kA/cm^2}$, which obscures the exact dependence of Z_{th} on temperature.

A peculiarity of our GaInNAsSb lasers with GaNAs barriers, not seen in GaInNAs/GaAs,[8] is that at very low current densities, Z does not asymptote to 1 but rather has a minimum and increases to $Z_0>1$ as J approaches zero. It was suggested[41] that the density of traps is so large that they are not completely filled at low currents. We believe that this might be the case, especially if the trap levels are located close to the QW conduction-band edge, e.g., the $(\mathrm{N–N})_{\mathrm{As}}$ split interstitial trap. The electron's quasi-Fermi level would be below the trap level at low biases, leading to only partial occupation of the electron trap. Instead of the recombination rate being proportional to the hole density, p, and the trap density, N_t, it would be proportional to p and some function of the electron density, e.g., $n^{1/3}$, since the number of occupied traps would increase sublinearly with electron concentration. This would lead to a value for Z_0 of 1.33. We define a quantity, J_{Trap}, as the current density at which the lowest region of the Z-J curve extrapolates to $Z=1$ [see Fig. 13(a)]. It approximates the current density required to fill the trap levels. These two features were investigated in the Fig. 12 simulation. $Z_0\approx1.3$ if the electron traps are located inside the band gap, 100 meV from the QW band edges, and N_t is small compared to N_c. Z_0 decreases from 2 to 1 and J_{Trap} decreases to zero as either the trap level location moves from the band edges to midband gap or the trap density decreases. The traps in curve (c) can be considered filled when curves (b) and (c) begin to overlap. From Fig. 12, we see that this occurs at approximately the same carrier density as the extrapolation of curve (c) to $Z=1$.

From the temperature-dependent Z-parameter data, we plot both Z_0 and J_{Trap} vs T_s in Fig. 13(b). From $T_s=15$ to 65 °C, Z_0 decreases slightly from 1.334 to 1.323 and J_{Trap} decreases from 238 to 190 $\mathrm{A/cm^2}$. At higher temperatures, the trap occupancy increases due to the broader Fermi–Dirac distribution and therefore both Z_0 and J_{Trap} are expected to decrease. A reduced trap level concentration for GaAs compared to GaNAs might explain why $Z_0=1$ for GaInNAs devices with GaAs barriers while $Z_0>1$ in our devices.

As the temperature is increased, the threshold density increases exponentially. At threshold, Z_{th} increases from 1.90 to 2.05 to 2.25 to 2.50 as T_s is increased from 15 to 45 °C in 10 °C steps. For comparison, Fehse *et al.*[8] report that Z_{th} increases from 2.1 to 2.4 in GaInNAs/GaAs at 1.3 μm and is roughly saturated at 2.9 in InGaAs/InP at 1.3 μm over the same 15–45 °C temperature range.

The temperature dependence of the recombination coefficients A, B, and C is expected to be,[8,20,42]

$$A\propto T^{1/2},\quad B\propto T^{-1},\quad C\propto\exp\left(-\frac{E_a}{k_BT}\right),\tag{8}$$

where E_a is the activation energy for the Auger process. C is a rapidly varying function of temperature; it is nearly zero but increases swiftly for $k_BT\ll E_a$ before saturating for $k_BT\gg E_a$. Near room temperature, the monomolecular coefficient A was observed to saturate in GaInNAs at 1.3 μm[8] due to the saturation of the thermal velocity, so we will assume that A is approximately constant for GaInNAsSb at 1.5 μm as well.

At low carrier densities, monomolecular and radiative recombination dominate, and since A is temperature insensitive and B decreases by $<15\%$ over the limited temperature range of the measurement, the low current density Z-J curves in Fig. 13(a) agree with this prediction of a temperature insensitive relationship. At and above $T_s=35\,^{\circ}\mathrm{C}$, where the threshold current density is above 1.5 $\mathrm{kA/cm^2}$ and Z_{th} exceeds 2.25, leakage and/or Auger recombination begin to dominate and the high current density portion of the Z-J curves should begin to separate with temperature due to the strong temperature dependence of these processes. This predicted feature is not visible in Fig. 13(a) because the data in this region are limited to a small temperature range $\Delta T=20\,^{\circ}\mathrm{C}$. A device with low thermal resistance and two antireflective coated facets to prevent heating and lasing, respectively, is needed to investigate this prediction further. Although Z should continue to increase with J above 1.5 $\mathrm{kA/cm^2}$ at low temperature, the rate of increase should be less than at high temperature.

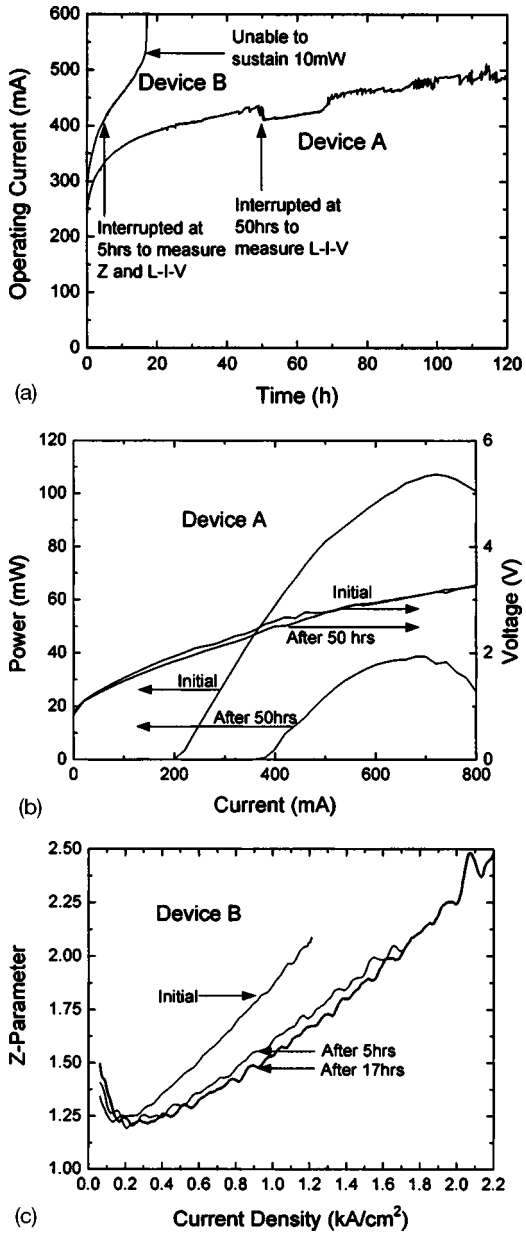

FIG. 14. (a) is the operation current vs time for two 20×1000 μm^2 devices at 10 mW cw. Device A, which had a better pretest performance, survived over 120 h of operation at $T_s=15$ °C, while device B only lasted 17 h at $T_s=20$ °C. (b) is the cw *L-I–V* curves before life testing and after 50 h for device A. (c) is the *Z-J* curves for device B. During life testing, the *Z* parameter at fixed *J* is reduced and Z_0 and J_{Trap} both increase. These three changes indicate an increase in the trap density during life testing.

RELIABILITY

A 20×1000 μm^2 laser, labeled device A, was operated at $T_s=15$ °C at 10-mW cw output power for 120 h. The time evolution of the operating current, I_{op}, is the lower curve of Fig. 14(a). Notice the sharp increase in current during the first 10 h, followed by a slower gradual increase. Part of the current increase is due to device heating. After 50 h, life testing was interrupted to remeasure the cw light-current–voltage (*L-I–V*) curves, which are plotted in Fig. 14(b). Device performance metrics are listed in Table III. Both the threshold and efficiency were degraded and the thermal rollover current was reduced slightly. The *V–I* curve did not change significantly. After 122 hs of life testing, one of the probes accidentally lost contact and scratched the sample and we were unable to obtain reliable *L-I–V* measurements after the life test.

The high levels of monomolecular recombination, observed in the *Z*-parameter measurements, provide thermal energy that enhances defect propagation. The active region and barriers are expected to have numerous point defects since they are highly strained metastable alloys grown at low temperatures. During life testing, these point defects can diffuse and nucleate extended defects that can propagate. This further accelerates device failure by increasing the number of nonradiative recombination sites. Since the defects relieve strain, the defect creation rate might be large initially but decrease over time leading to a slower gradual increase in I_{op}.

To investigate this further, life testing was conducted on a similar 20×1000 μm^2 laser, device B, also operated at 10-mW cw output power, but at $T_s=20$ °C and a *Z*-parameter measurement and pulsed and cw *L-I–V* measurements were conducted before and during life testing. Device B had a slightly worse pretest threshold and efficiency than device A and was also operated at $T_s=20$ °C instead of 15 °C (see Table III). It was only able to sustain 10-mW cw for 17 h, as shown in the upper curve of Fig. 14(a). Again, a sharp increase in current was observed during the first 10 h, but because of the higher T_a and I_{op}, the device failed before the slower gradual increase was observed. The changes to the cw *L-I–V* curves during life testing were similar to those for device A, but occurred more rapidly. The degradation to the pulsed mode *L-I–V* curves was less noticeable.

The *Z-J* curves for device B before life testing, after 5 and 17 h, are displayed in Fig. 14(c). At a fixed current

TABLE III. Performance metrics during life testing for two 20×1000 μm^2 devices at 10-mW cw. Device A had $T_s=15$ °C; device B had $T_s=20$ °C. After 50 h, the cw threshold current increased by 79% and external differential quantum efficiency decreased by 39% of their respective pretest values for device A. Device B showed a 90% threshold increase and 69% efficiency decrease in cw mode after only 17 h, but it had only a 55% threshold increase and 24% efficiency decrease in pulsed mode. Z_0 and J_{Trap} both increase during life testing.

Device	Time (h)	$J_{10\ \mathrm{mW}}$ (kA/cm^2)	T_a (°C)	$J_{\mathrm{th}}^{\mathrm{cw}}$ (kA/cm^2)	η_e^{cw} (%)	$P_{\mathrm{max}}^{\mathrm{cw}}$ (mW)	$J_{\mathrm{th}}^{\mathrm{PUL}}$ (kA/cm^2)	η_e^{PUL} (%)	Z_{th}	Z_0	J_{Trap} (kA/cm^2)
A	0	1.25	30	1.05	38	107	⋯	⋯	⋯	⋯	⋯
A	50	2.12	48	1.88	23	39	⋯	⋯	⋯	⋯	⋯
A	120	2.43	50	⋯	⋯	⋯	⋯	⋯	⋯	⋯	⋯
B	0	1.43	36	1.18	35	67	0.97	41	2.05	1.48	0.212
B	5	2.05	48	1.79	22	26	1.34	35	2.05	1.57	0.233
B	17	2.63	59	2.24	11	4.5	1.50	31	2.53	1.63	0.254

density, the Z parameter is reduced over time and the Z-J curve remains closer to $Z=1$, indicating an increase in the monomolecular recombination current. The value of Z_{th} increases over time from 2.05 to 2.58 after 17 h due to the increase in T_a at threshold from 33 to 50 °C. From the Z-J curves, we estimate that the monomolecular current density increased by approximately 0.45 $\mathrm{kA/cm^2}$ at threshold over 17 h. This agrees with the observed 0.53-$\mathrm{kA/cm^2}$ increase in the total pulsed threshold density. Thus, additional device heating causes the other half of the 1.06-$\mathrm{kA/cm^2}$ increase in cw threshold.

Z_0 and J_{Trap} both increased during life testing. The rise of Z_0 indicates a reduction in the trap occupation probability and the rise in J_{trap} indicates that higher currents are needed to fill the traps. These two changes can be caused by three things: (1) an increase in the $(\mathrm{N–N})_{\mathrm{As}}$ trap density, (2) an increase in the trap energy position relative to the QW band edge, or (3) an increase in the $(\mathrm{As–N})_{\mathrm{As}}$ trap recombination. However, only the first case would lead to the Z-J curve remaining closer to $Z=1$. Thus, we conclude that the primary source of device degradation is an increase in $(\mathrm{N–N})_{\mathrm{As}}$ trap recombination and that the degradation is more pronounced in cw operation because of device heating.

On a similar device, C, the TSE spectrum at constant density of 3 $\mathrm{kA/cm^2}$ at $T_s=70$ °C ($T_s=115$ °C) was collected for 6 h. The emission rate for the $\mathrm{E^1\text{-}HH^1}$, $\mathrm{E^1\text{-}HH^3}$, $\mathrm{E^2\text{-}HH^2}$, and $(\mathrm{E\text{-}LH})_{\mathrm{Barrier}}$ and 800-meV transitions decreased by 6%, 9%, 11%, 16%, and 9%, respectively. The extra reduction in the higher-order transitions indicates a lower overall carrier density at fixed current. Pre/post-Z-parameter measurements again show increased monomolecular recombination. Since the 800-meV emission peak did not increase in strength, we conclude that the peak is not caused by a radiative transition from the $(\mathrm{N–N})_{\mathrm{As}}$ trap level, as was initially suspected, but is instead the exciton peak.

There is a heating-induced feedback that drastically increases operation current and device degradation during constant power cw operation. An increase in nonradiative recombination elevates T_a due to the electrical and thermal resistances. Increased T_a reduces gain and thus increases the threshold current, which is already mostly nonradiative. This increases T_a again and the new steady-state operating current is much higher than indicated by the simple small increase in nonradiative current. Further, the trap creation rate increases due to the increases in T_a and nonradiative current. By mounting the devices episide down, the thermal resistance can easily be reduced by two- to threefold for ridge waveguide devices and four- to sixfold for broad area (>50 μm wide) devices. Combined with a lower series resistance design, this avalanche effect can be mitigated. Also, by reducing nonradiative recombination from barrier traps, i.e., using GaAs barriers, improving the material quality of GaNAs barriers, or increasing the barrier height, device lifetimes comparable to the 1000 h at 1.5 W of cw power in 1.3-μm GaInNAs (Ref. 12) can be expected for GaInNAsSb at 1.5 μm.

CONCLUSION

The spontaneous emission measurements performed below and above threshold indicate the presence of large amounts of nonradiative recombination and the failure of the radiative recombination rate to strongly clamp at threshold. At room temperature, nonradiative recombination represents 80% of the threshold current, while at elevated temperatures, carrier leakage or Auger recombination become dominant because of their strong dependence on temperature and carrier concentration. The weak clamping of the quasi-Fermi levels above threshold allows additional recombination to occur, reducing the internal efficiency.

The multisection gain technique was adapted to obtain absorption data and provide accurate measurements of the band gap, band offsets, and effective masses of GaInNAsSb. Although the relatively even split in the electron/heavy-hole band offsets is favorable, the effective barrier heights might be too small to prevent thermionic escape of both types of carriers at high temperatures.

Z-parameter measurements confirm that an increase in monomolecular recombination is responsible for device degradation during life testing. The degradation is much worse in cw mode than pulsed due to device heating. GaAs barriers would provide better carrier confinement and should have fewer barrier defects than GaNAs barriers. Both features will reduce monomolecular recombination. A multiple quantum well (MQW) laser will have stronger optical confinement. This will lower the threshold carrier density and reduce leakage and Auger recombination. Mounting episide down can minimize device heating. With these changes, the present deficiencies can be eliminated and even lower threshold, higher efficiency, and more reliable GaInNAsSb lasers are expected.

ACKNOWLEDGMENTS

The authors would like to thank Professor A. R. Adams at the University of Surrey, Professor N. Tansu at Lehigh University, and D. P. Bour of Agilent Technologies for discussions regarding Auger recombination, carrier leakage, IVBA, and the Z parameter. The authors also wish to thank S. Zou of Santur Corp. for assistance in wafer thinning and facet coatings. The authors acknowledge A. Moto of Sumitomo Electric Industries for helpful discussions and donation of substrates. This work was supported under Grant Nos. ARO DAAD17-02-C-0101, DARPA MDA972-00-1-0024, NSF PHY-01-40297, and ARO DAAD19-02-1-0184, as well as the Stanford Network Research Center (SNRC). One of the authors (L.L.G.) acknowledges support from a National Physical Science Consortium Fellowship and stipend support from Xerox Palo Alto Research Center. Three of the authors (S.R.B., M.A.W., and H.B.Y.) each acknowledge Stanford University and NSF fellowship support over the years.

[1] S. Bank, M. Wistey, H. Yuen, L. Goddard, W. Ha, and J. S. Harris, Jr., Electron. Lett. **39**, 1445 (2003).
[2] S. Bank, M. Wistey, L. Goddard, H. Yuen, V. Lordi, and J. S. Harris, Jr., IEEE J. Quantum Electron. **40**, 656 (2004).
[3] M. Wistey, S. Bank, H. Yuen, L. Goddard, and J. S. Harris, Electron. Lett. **39**, 1822 (2003).
[4] S. Bank, M. Wistey, L. Goddard, H. Yuen, H. Bae, and J. S. Harris, Jr., Electron. Lett. **40**, 1186 (2004).
[5] L. Goddard, S. Bank, M. Wistey, H. Yuen, H. Bae, and J. S. Harris, Jr., LEOS Annual Meeting Conference Proceedings (IEEE, Piscataway, NJ, 2004), Vol. 1, pp. 144-145.

[6]R. Averbeck, G. Jaschke, L. Geelhaar, and H. Riechert, J. Cryst. Growth (to be published).
[7]R. Fehse, S. Jin, S. Sweeney, A. Adams, E. O'Reilly, H. Riechert, S. Illek, and A. Egorov, Electron. Lett. **37**, 1518 (2001).
[8]R. Fehse, S. Tomić, A. Adams, S. Sweeney, E. O'Reilly, A. Andreev, and H. Riechert, IEEE J. Sel. Top. Quantum Electron. **8**, 801 (2002).
[9]A. Phillips, S. Sweeney, A. Adams, and P. Thijs, IEEE J. Sel. Top. Quantum Electron. **5**, 401 (1999).
[10]H. Riechert, A. Egorov, D. Livshits, B. Borchert, and S. Illek, Nanotechnology **11**, 201 (2000).
[11]I. Vurgaftman and J. Meyer, J. Appl. Phys. **94**, 3675 (2003).
[12]D. Livshits, A. Egorov, and H. Riechert, Electron. Lett. **36**, 1381 (2000).
[13]M. Kondow, T. Kitatani, K. Nakahara, and T. Tanaka, Jpn. J. Appl. Phys., Part 2 **38**, L1355 (1999).
[14]M. Itoh, H. Sugiura, H. Yasaka, Y. Kondo, K. Kishi, M. Fukuda, and Y. Itaya, Appl. Phys. Lett. **72**, 1553 (1998).
[15]I. Vurgaftman, J. Meyer, and L. Ram-Mohan, J. Appl. Phys. **89**, 5815 (2001).
[16]P. Thijs, L. Tiemeijer, P. Kuindersma, J. Binsma, and T. Dongen, IEEE J. Quantum Electron. **27**, 1426 (1991).
[17]P. Krispin, V. Gambin, J. S. Harris, and K. Ploog, J. Appl. Phys. **93**, 6095 (2003).
[18]S. Chuang, *Physics of Optoelectronic Devices*, 1st ed. (Wiley, New York, 1995), p. 351.
[19]D. Ahn and S. Chuang, IEEE J. Quantum Electron. **30**, 350 (1994).
[20]A. Haug, Appl. Phys. B: Photophys. Laser Chem. **44**, 151 (1987).
[21]J. Thomson, H. Summers, P. Hulyer, P. Smowton, and P. Blood, Appl. Phys. Lett. **75**, 2527 (1999).
[22]W. Shan, W. Walukiewicz, J. Ager, E. Haller, J. Geisz, D. Friedman, J. Olson, and S. Kurtz, J. Appl. Phys. **86**, 2349 (1999).
[23]M. Ya, Y. Chen, and Y. Huang, J. Appl. Phys. **92**, 1446 (2002).
[24]Y. Zhang, A. Mascarenhas, H. Xin, and C. Tu, Phys. Rev. B **61**, 4433 (2000).
[25]S. Tomić, E. O'Reilly, P. Klar, H. Gruning, W. Heimbrodt, W. Chen, and I. Buyanova, Phys. Rev. B **69**, 245305 (2004).
[26]H. Schneider and K. v. Klitzing, Phys. Rev. B **38**, 6160 (1988).
[27]R. Kudrawiec, H. Yuen, K. Ryczko, J. Misiewicz, S. Bank, M. Wistey, H. Bae, and J. S. Harris, Jr., J. Appl. Phys. **97**, 053515 (2005).
[28]L. Coldren and S. Corzine, *Diode Lasers and Photonic Integrated Circuits*, 1st ed. (Wiley, New York, 1995), p. 138.
[29]L. Goddard, S. Bank, M. Wistey, H. Yuen, and J. S. Harris, Jr., Proc. SPIE (to be published).
[30]S. Chuang, *Physics of Optoelectronic Devices*, 1st ed. (Wiley, New York, 1995), pp. 427–428.
[31]P. Smowton and P. Blood, IEEE J. Sel. Top. Quantum Electron. **3**, 491 (1997).
[32]P. Smowton and P. Blood, Appl. Phys. Lett. **70**, 2365 (1997).
[33]S. Bank, L. Goddard, M. Wistey, H. Yuen, and J. S. Harris, Jr., IEEE J. Sel. Top. Quantum Electron. (submitted).
[34]S. Sweeney, A. Phillips, A. Adams, E. O'Reilly, and P. Thijs, IEEE Photonics Technol. Lett. **10**, 1076 (1998).
[35]L. Goddard, S. Bank, M. Wistey, H. Yuen, and J. S. Harris, Jr., *CLEO/IQEC and PhAST Technical Digest* on CD-ROM (The Optical Society of America, Washington, DC, 2004), CTuP22.
[36]R. Olshansky, C. Su, J. Manning, and W. Powazinik, IEEE J. Quantum Electron. **QE-20**, 838 (1984).
[37]D. Bour, D. Treat, R. Thornton, R. Geels, and D. Welch, IEEE J. Quantum Electron. **29**, 1337 (1993).
[38]V. Chazapis, H. Blom, K. Vodopyanov, A. Norman, and C. Phillips, Phys. Rev. B **52**, 2516 (1995).
[39]N. Dutta, J. Appl. Phys. **54**, 1236 (1983).
[40]A. Haug, Solid-State Electron. **21**, 1281 (1978).
[41]A. R. Adams (personal communication).
[42]A. Haug, J. Phys. Chem. Solids **49**, 599 (1988).